



Article

Black-Grass Monitoring Using Hyperspectral Image Data Is Limited by Between-Site Variability

Robert M. Goodsell ^{1,*}, Shaun Coutts ², William Oxford ³, Helen Hicks ⁴ , David Comont ⁵ , Robert P. Freckleton ¹ and Dylan Z. Childs ¹

¹ Ecology and Evolutionary Biology, School of Biosciences, University of Sheffield, Sheffield S10 2TN, UK; robert.p.freckleton@sheffield.ac.uk (R.P.F.); dylan.childs@sheffield.ac.uk (D.Z.C.)

² Lincoln Institute for Agri-Food Technology, College of Science, Lincoln LN2 2BJ, UK; scoutts@lincoln.ac.uk

³ 2Excel Aviation Ltd., Hangar 3, Fourth Avenue, Doncaster DN9 3GE, UK; william.oxford@2excel.uk

⁴ School of Animal Rural & Environmental Sciences, Nottingham Trent University, 50 Shakespeare St., Nottingham NG1 4FQ, UK; helen.hicks@ntu.ac.uk

⁵ Rothamsted Research, Harpenden, Hertfordshire AL5 2JQ, UK; david.comont@rothamsted.ac.uk

* Correspondence: robert.m.goodsell@gmail.com

Abstract: Many important ecological processes play out over large geographic ranges, and accurate large-scale monitoring of populations is a requirement for their effective management. Of particular interest are agricultural weeds, which cause widespread economic and ecological damage. However, the scale of weed population data collection is limited by an inevitable trade-off between quantity and quality. Remote sensing offers a promising route to the large-scale collection of population state data. However, a key challenge is to collect high enough resolution data and account for between-site variability in environmental (i.e., radiometric) conditions that may make prediction of population states in new data challenging. Here, we use a multi-site hyperspectral image dataset in conjunction with ensemble learning techniques in an attempt to predict densities of an arable weed (*Alopecurus myosuroides*, Huds) across an agricultural landscape. We demonstrate reasonable predictive performance (using the geometric mean score-GMS) when classifiers are used to predict new data from the same site (GMS = 0.74-low density, GMS = 0.74-medium density, GMS = 0.7-High density). However, even using flexible ensemble techniques to account for variability in spectral data, we show that out-of-field predictive performance is poor (GMS = 0.06-low density, GMS = 0.13-medium density, GMS = 0.08-High density). This study highlights the difficulties in identifying weeds in situ, even using high quality image data from remote sensing.

Keywords: black-grass; machine learning; weeds; hyperspectral imagery



Citation: Goodsell, R.M.; Coutts, S.; Oxford, W.; Hicks, H.; Comont, D.; Freckleton, R.P.; Childs, D.Z. Black-Grass Monitoring Using Hyperspectral Image Data Is Limited by Between-Site Variability. *Remote Sens.* **2024**, *16*, 4749. <https://doi.org/10.3390/rs16244749>

Academic Editors: Clement Atzberger and Kevin Tansey

Received: 11 October 2024

Revised: 12 December 2024

Accepted: 16 December 2024

Published: 20 December 2024



Copyright: © 2024 by the authors. Licensee MDPI, Basel, Switzerland. This article is an open access article distributed under the terms and conditions of the Creative Commons Attribution (CC BY) license (<https://creativecommons.org/licenses/by/4.0/>).

1. Introduction

Managing weed populations is a major focus of agroecology due to their severe ecological and economic impacts. However, targeting and prioritising management, and tracking efficacy requires that weeds are monitored over large scales [1–3]. Unfortunately, estimating weed abundance across landscapes, catchments, and bio-geographic regions is expensive in terms of time and resources. The consequence is that most studies of weed responses to management collect data from a few locations that span a narrow range of environmental conditions [4–6]. In contrast, weed populations typically have large geographic ranges and are subject to considerable variability in their environment and management histories [1]. This variation in local conditions drives variation in population performance and responses to management [7–13]. Thus, understanding the processes that shape weed populations over large spatial scales is necessary to predict their population dynamics and plan effective management. To achieve this goal, the scale of ecological data collection must expand to provide sufficient data to parameterise ecological models that are validated and applicable across entire population ranges.

Remote sensing (the collection of information through automated or non-contact recording) offers a promising route to facilitate rapid, large-scale, and cost-effective data collection across a variety of landscapes [14–17]. However, a key challenge in agroecology is deriving measures of weed abundance or population size from such data [15,18]. Obtaining reliable population estimates from remote sensing data is difficult due to the complexity of ecological systems. Populations often exist in communities consisting of closely related species and those that bear a high resemblance to one another, making discrimination between organisms extremely challenging [19,20]. This is also true for weed populations, where discrimination between the crop and pest may be difficult to achieve [18]. Despite this, several studies have demonstrated the capability to identify weed populations and even produce estimates of population size using remote sensing data [8,15,19–25].

Many agricultural weed studies focus on only a few locations, lacking data collection over a range of environments [26–29]. Additionally, they often do not validate approaches by testing prediction accuracy with out of sample data from new sites. The problem is that the distribution of populations across a landscape with varying environmental conditions [25,30,31] and variability in the state of individual organisms [32,33] will affect the spectral properties of image data and the ability to identify organisms accurately. In particular, when detecting weeds in an arable field, differences in crop cultivar might be expected to have a pronounced impact on the spectral properties of the crop, as will factors like water stress, growth stage, and pathogens, compromising the generalisability of detection algorithms trained on only a few locations. Similarly, the extent of genetic and morphological variability amongst separate weed populations is still relatively unexplored, but even small differences might play an important role in altering the reflective spectral properties relative to the crop.

Studies with restricted temporal or spatial scope will have limited performance when estimating population size in previously un-surveyed sites. Training data with small sample sizes will contain a limited range of ambient conditions from which to build predictive models that are robust to environmental heterogeneity. However, even studies with large-scale data collection achieve low out-of-sample accuracy. Lambert et al. [14] combined large-scale unmanned aerial vehicle (UAV) imagery from over 100 fields with machine learning pipelines to classify densities of weeds in arable wheat fields in the UK. Their key finding was that classification accuracy was high when models were applied to predict new observations within a field, but dropped dramatically when used to classify density at an entirely new site. For remote sensing data to be useful in assessing population size, any approach must be generalisable to new locations [34].

Aside from ensuring that training data are sufficiently representative of the entire population, one option to increase out-of-site identification accuracy is to improve the quality of the image data itself. Aerial collection is the most practical method to collect data at the required scale, but this imposes a trade-off between image resolution and the scale of collection. Even a 1 cm resolution requires low-flying UAV's, which limits collection scale [35]. Another way to increase the information content of the images is to capture a wider band of the light spectrum. Many studies use data that consist of red–green–blue (RGB) or multi-spectral images, which are low bandwidth and have limited coverage in the visible light spectrum [14,15,36]. Low bandwidth data may not contain enough information or the frequencies relevant to the study organism, which allow accurate identification across multiple sites. In practice, therefore, multispectral imagery does not always provide an additional benefit over RGB images for detecting or quantifying weed populations [21]. Alternatively, hyperspectral (HS) imagery provides much higher coverage of visible light and near-infrared frequencies and could improve the opportunity for successful signal detection of target organisms [26–28,37–39].

As well as appropriate survey design and good quality data, a key consideration are the steps involved in building a reliable analytical pipeline. Studies have often used single-model approaches, where one model is trained on all available data except a validation set [15,38,40–42]. Given that high environmental and population-level variability can

impact accuracy, a single model may perform poorly for new sites at the extremes or outside of the observed conditions [34,43]. The alternative is to use ensemble-based methods, where multiple models are trained on groups of data [44]. For example, models are trained on spatially aggregated data from each survey site, and then individual predictions from each model are combined to provide an overall prediction for the new data. The primary advantage of this method is the introduction of flexibility, as predictions of individual models can be weighted based on criteria that could improve predictive performance.

This paper combines large-scale survey data with hyperspectral imagery and machine learning classifiers to predict the density of plant populations across multiple spatial extents. We focus on populations of black-grass (*Alopecurus myosuroides*, Huds.) which is a particularly damaging arable weed in the UK. We investigate the efficacy of using raw hyperspectral (HS) and vegetation indices (VGI) data derived from HS bands in conjunction with an ensemble learning method to classify weed density, both within and out of field. Here, we aimed to compare whether out-of-field performance can be improved by the combination of ensemble learning and high-bandwidth image data.

2. Materials and Methods

2.1. Weed Density Data

To assess the feasibility of large-scale weed identification we used data from a nationwide black-grass monitoring network. This project encompassed over 200 fields from over 70 farms in England and was established to monitor the impact of black-grass on UK agriculture. We employed a density-structured framework [2,7,45] to collect information on weed density across arable farms in England, using surveys conducted as part of a study on the prevalence of black-grass across the UK. Weeds were surveyed in winter wheat fields over June–July, when flowering, as at this timepoint the emerged weed flower-heads are readily distinguished from the crop by eye. The survey methodology collected an abundance of information as a series of categorical density states, where fields were divided into a series of 20 m by 20 m quadrats, and the weeds were classified as one of a series of density states. In this study, we condensed density states into three categories, absent to low (L), medium (M), and high (H), which contained both high and very-high categories from the surveys. This simplifies the prediction task, whilst retaining enough information critical to management, as only densities of ‘medium’ and above impact yield [46–48]. This framework has several advantages, firstly it allows rapid collection across landscapes, which allows a large-scale evaluation of weed populations on the ground. Secondly, data collection in this manner simplifies the identification problem into classification rather than estimates of continuous abundance, where the margin of error is higher, whilst still permitting estimates to be incorporated into models of population dynamics [2,3,45]. We collected density-state observations from 31 fields spread across England (Figure 1), consisting of 3342 quadrat-level assessments of weed densities. We collected hyperspectral data for these same fields.

2.2. Remote Sensing Data

Hyper-spectral data collection was completed during June and July in 2018. Flights were undertaken using a manned fixed-wing aircraft flying at approximately 1km above ground level. Flights yielded data with 0.32 m ground sample distance (GSD, i.e., 1 pixel is 32 cm × 32 cm resolution) in the visible and near-infrared spectra and 0.72–0.66 m GSD in the short-wave infrared spectra. Multispectral images were collected using a PhaseOne iXA180 colour survey camera (PhaseOne, Copenhagen, Denmark), and hyperspectral images with NEO Hypspx VNIR-1800/SWIR-384e (Hypspx, Wellington, FL, USA) cameras. See Table S2 for full camera specifications. Navigation processing included corrections made using the Ordnance survey receiver independent ex-change format network.

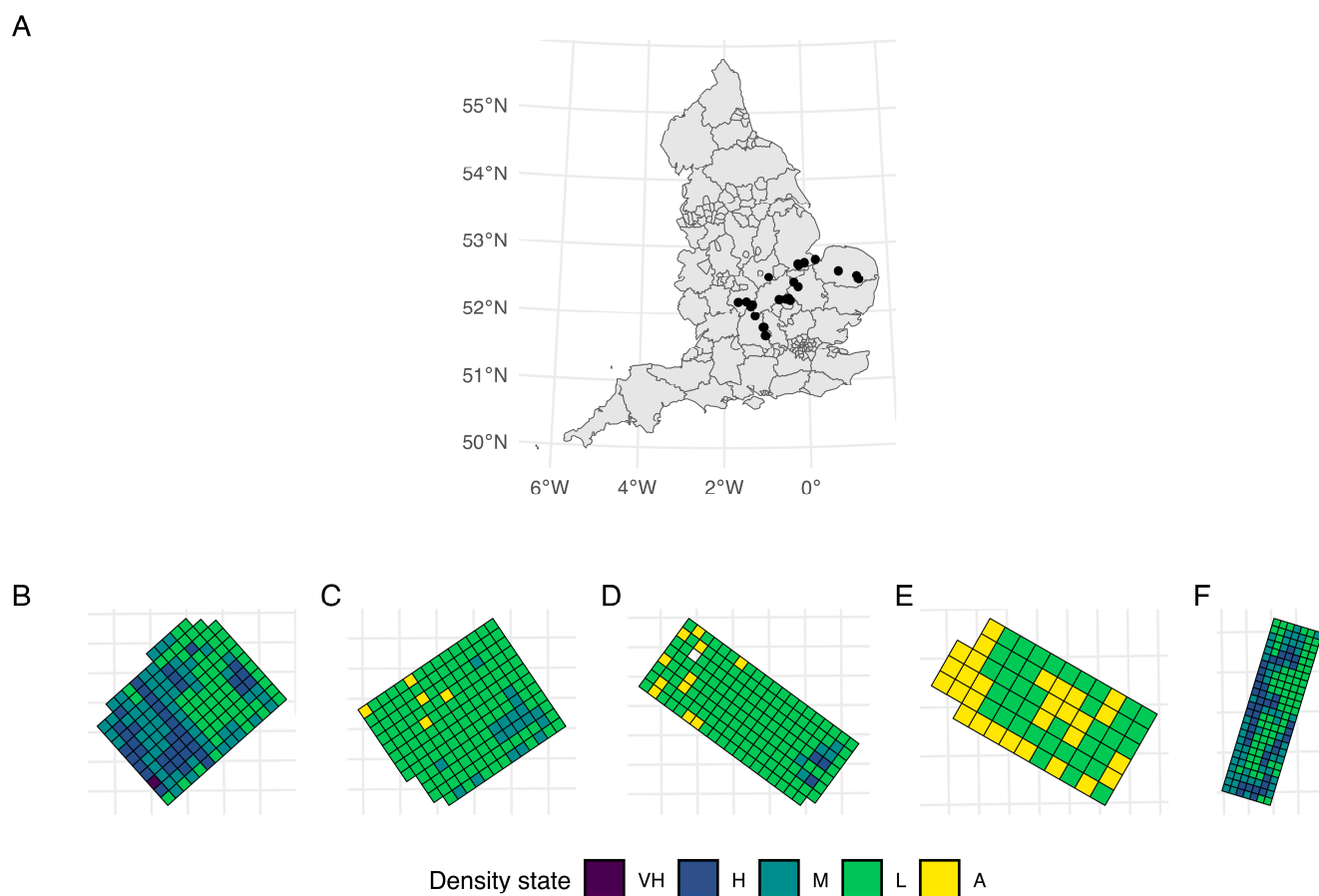


Figure 1. (A) The location of the 31 fields at which both weed density state and hyperspectral image data were collected in England. (B–F) Examples of weed density state distributions in 5 example fields in the dataset, colours represent different density states (Absent, Low, Medium, High, and Very High). Each quadrat represents a 20 m × 20 m area in which weed density was assessed and classified into one of the five density states.

Photogrammetric processing and the creation of mosaic images was achieved using Correlator3D software (v8.0.) [49]. Hyperspectral images were radiometrically calibrated using NEO software (v2.0) and spatially calibrated to an Ordnance Survey 50 m digital elevation model, using the software PARGE (v2.5) [50]. Calibrated hyperspectral images were aligned at sub-pixel level to the multispectral mosaic captured by the PhaseOne camera using an image matching algorithm. Atmospheric correction was achieved using quick atmospheric correction (QUAC), implemented within the ENVI software v(5.4). Savitzky–Golay smoothing was applied to all spectra (with a window length of 11 and polynomial order of 3) to reduce signal noise before analysis [1].

2.3. Pre-Processing

We produced two datasets for classification from the raw hyperspectral data. The first consisted of 98 bands of hyperspectral data for each field surveyed, ranging from 416 nm in wavelength (short wavelength visible light), to 991 nm (near-infrared). We normalised these data for each field by dividing by the median value within each band. The second dataset consists of 18 vegetation indices, which were calculated from the hyperspectral data (Table 1). The outer sets of quadrats in each field were removed from the analysis to remove any potential artefacts created by surrounding vegetation in the field margins.

Table 1. Vegetation indices calculated from hyperspectral data. Numbers represent the reflectance (R) wavelength of a spectral band in nanometres (nm). Where they appear, NIR, Red, Green, Blue, and Yellow refer to near-infrared (800–2500 nm), red (620–800 nm), green (500–620 nm), blue (450–500 nm), and yellow wavelengths (570–580 nm) of the spectrum, respectively.

Name	Formula	Reference
Anthocyanin reflectance index 2	$ARI2 = R_{800} \times \left(\frac{1}{R_{550}} - \frac{1}{R_{700}} \right)$	[51]
Carotenoid reflectance index 1	$CRI1 = \frac{1}{R_{510}} - \frac{1}{R_{550}}$	[52]
Modified red edge NDVI	$MRENDVI = R_{800nm} \left(\frac{R_{750} - R_{705}}{R_{750} + R_{705} \times R_{445}} \right)$	[53]
Modified soil adjusted vegetation index	$MSAVI = 2NIR + 1 - \sqrt{(2NIR + 1)^2 - 8}$	[54]
Normalised difference vegetation index	$NDVI = \frac{NIR - Red}{NIR + Red}$	[55]
Photochemical reflectance index	$PRI = \frac{R_{531} - R_{570}}{R_{531} + R_{570}}$	[56]
Red edge position index	$REPI = 700 + 40 \left(\frac{\left(\frac{R_{670} + R_{780}}{2} \right) - R_{700}}{R_{740} - R_{700}} \right)$	[57]
Red–green ratio	$RGR = \frac{Red}{Green}$	
Structure insensitive pigment index 1	$SIP1 = \frac{R_{800} - R_{445}}{R_{800} - R_{680}}$	[58]
Transformed chlorophyll absorption reflectance index	$TCARI = 3[(R_{700} - R_{670}) - 0.2(R_{700} - R_{550}) \times (R_{700} \times R_{670})]$	[59]
Optimised soil adjusted vegetation index	$OSAVI = 1 + Yellow \left(\frac{R_{800} - R_{670}}{R_{800} - R_{670} + Yellow} \right)$	[60]
Triangular vegetation index	$TVI = \frac{120(R_{750} - R_{550}) - 200(R_{670} - R_{550})}{2}$	[61]
Vogelmann Red edge 1	$VREI1 = \frac{R_{740}}{R_{720}}$	[62]
Water band index	$WBI = \frac{R_{970}}{R_{900}}$	[63]
Plant biochemical index	$PBI = \frac{R_{810}}{R_{560}}$	
Plant senescence reflectance index	$PSRI = \frac{R_{680} - R_{500}}{R_{750}}$	[64]
Red edge area 2	$REA2 = \frac{(R_{708} \cdot R_{716}) - (R_{676} \cdot R_{685})}{(R_{708} \cdot R_{716}) + (R_{676} \cdot R_{685})}$	[65]
Visible atmospherically resistant index	$VARI = \frac{Green - Red}{Green + Red - Blue}$	[66]

2.4. Analysis

We present a full workflow diagram of our end-to-end pipeline, from feature extraction to classification, in Figure 2. We trained random forests [67] to predict the density state (low: L, medium: M, high: H) of each quadrat using pixel-level hyperspectral (HS) or VGI data. Random forests are machine learning algorithms commonly applied in classification tasks. They reduce overfitting and improve predictive accuracy by averaging the results from a large number of individual decision trees built during fitting, making them a robust choice for high-dimensional and noisy biological data. To reduce the computational size of the task, we sampled 1000 pixels from each of the 3342 quadrats in both the HS and VGI feature sets. Each pixel was assigned the weed density class of the quadrat to which it belongs.

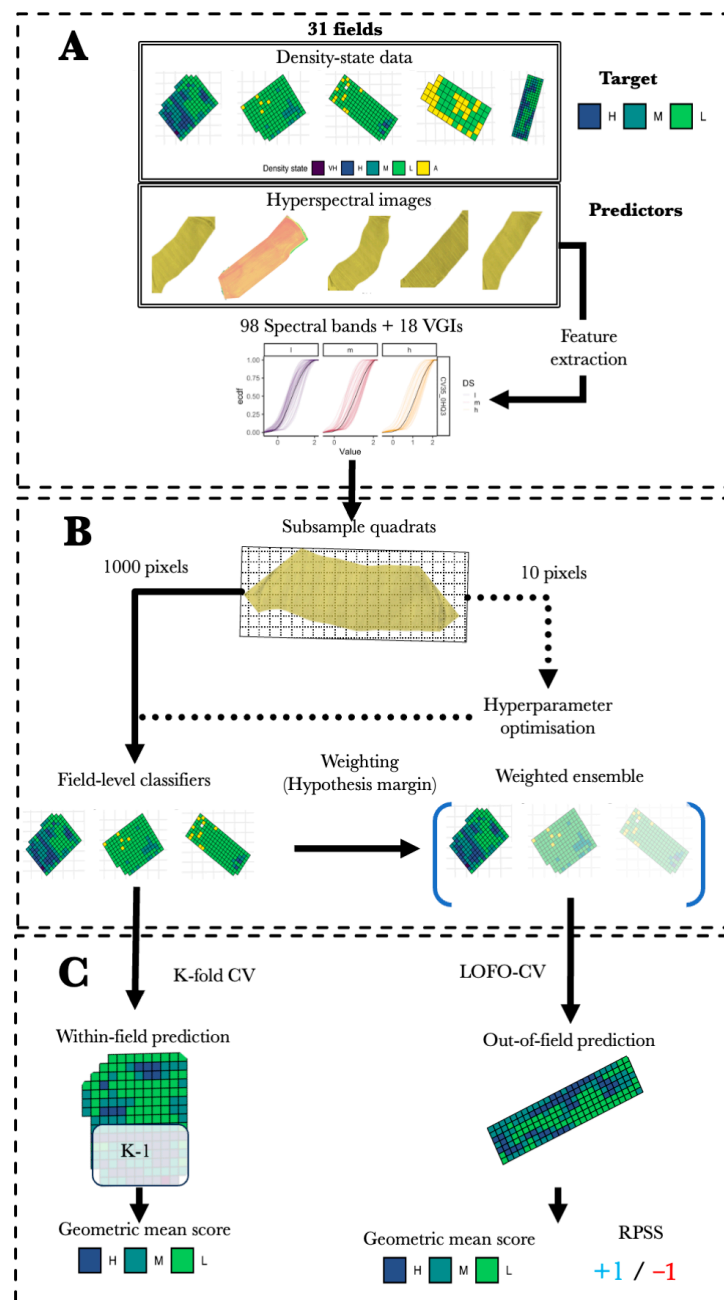


Figure 2. An end-to-end workflow of the full analysis presented in this paper. **(A)** An overview of the raw data collected from 31 fields across England, including the density-state data (i.e., the prediction target), and the raw hyperspectral data. From the raw hyperspectral data we extract two feature sets, one consisting of 98 hyperspectral bands (the HS feature set), and one consisting of 98 commonly used vegetation indices (VGI feature set). **(B)** An overview of the model fitting procedure. Hyperparameter optimisation was undertaken on a subset of data (subsampling 10 pixels for each quadrat in each field), which were then used in the main model fitting step. A random forest classifier was fit to each individual field and a weighted ensemble was built by weighting classifiers by their spectral similarity to the target field in the out-of-sample prediction task. **(C)** Prediction and validation comprised two components. First, within-field performance was assessed using K-fold cross-validation and the geometric mean score (GMS) was used to provide a measure of accuracy for each density-state. Second, out-of-sample prediction was assessed using leave-one-field-out cross-validation (LOFO-CV) on a field not included in the ensemble. The GMS and ranked probability skill score (RPSS), were used to assess state-level and field-level predictive performance, respectively.

We performed hyperparameter optimisation for the random forests in the form of a simple grid search across a series of hyperparameter combinations detailed in Table S1 (Supplementary Materials). For each hyperparameter combination, we fitted random forests to a subset of data (10 pixels for each quadrat) and for each combination of hyperparameters we performed leave-two-fields-out cross-validation by holding out pairs of fields and refitting the model to each set of data. Hyperparameters were selected by taking the parameter combinations that had the best predictive performance (assessed using ranked probability skill score) averaged over held-out data. Averaging the values across each held-out fold of our data ensures that we have a good ‘overall’ performing set of hyperparameters for the classification task. These hyperparameters were then used in the subsequent analyses to predict black-grass density. Model fitting was implemented in the ranger package in R [68]. All 26 individual classifiers were run on the Sheffield Advanced Research Cluster (ShARC) and specified to run using 128 GB of RAM on Intel Xeon E5 processors (2.4 GHz base frequency).

2.5. Ensemble Learning

We classified density states from HS and VGI data by training individual random forests, using the hyperparameters estimated above, to each of the 20 fields, with representation of at least two density states. The same hyperparameter combinations were used for all individual classifiers. As the density-state distribution was skewed towards low states ($L = 2300$, $M = 525$, $H = 517$) and all single-state fields within our data consisted entirely of ‘low’ density states, we removed these fields (totalling 11 in number) from the ensemble to reduce the risk of incorrect classifications due to class imbalance.

We assessed predictive performance for individual field-level classifiers by conducting k -fold ($k = 5$) cross-validation on unseen observations within fields. To evaluate prediction quality for new fields, we assessed the performance of classifiers in an ensemble via leave-one-field-out cross-validation (LOFO-CV) [34], using HS data from the total set of 31 fields. Each field-level classifier made a pixel-level prediction in the form of a vector of probabilities for each density state and the state with the highest probability was classed as the pixel-level prediction. An ensemble of all field-level classifiers (except the one held out as the validation field), was then used to ‘vote’ on the final prediction for the state of a quadrat, with the winning density state being the state with the most votes. To account for environmental variability, we weighted the votes of classifiers trained on data with higher spectral similarity to the data from the unseen field and compared their accuracy to an unweighted ensemble for reference.

We used hypothesis margins [69] to weight the predictions of classifiers based on how similar the spectral characteristics of the training field were to the characteristics of the unseen target field.

$$h(x_j) = 0.5 \left(\left| x_j - \text{near}_f(x_j) \right| - \left| x_j - \text{near}_j(x_j) \right| \right), \quad (1)$$

where x_j is a pixel in the unseen field j , and $\text{near}_f(x_j)$ is the nearest neighbour in the feature space of classifier field f . Therefore, $\text{near}_j(x_j)$ is the nearest neighbour in the feature space of the new field j . We then implemented weighting via:

$$w_f = \frac{\exp \left[-\alpha \left(H_{fj} - \hat{H}_j \right) \right]}{\sum_{\forall f} \exp \left[-\alpha \left(H_{fj} - \hat{H}_j \right) \right]} \quad (2)$$

where w_f is the weight applied to the prediction of classifier f , H_{fj} is the median hypothesis margin between classifier field f and unseen field j , and \hat{H}_j is the median of the minimum hypothesis margin between all classifier fields and unseen field j . α is the parameter controlling the size of the weights relative to the distance between spectral signatures of

the classifier and unseen fields. In this analysis we use $\alpha = 0$ for unweighted classifiers and $\alpha = 2 \wedge 10$ for weighted classifiers.

2.6. Assessing Performance

We assessed predictive performance through two metrics. To assess how well ensembles identified different density classes given an imbalanced class distribution (skewed towards low and medium states), we calculated the geometric mean score for each prediction:

$$G_k = \sqrt{n_{ik}t_{ik}} \quad (3)$$

where n_{ik} and t_{ik} are the true negative rate (i.e., proportion of quadrats where an observation was correctly predicted to be a state other than state k) and positive rate (proportion of quadrats where a state was correctly predicted to be state k), respectively, of state k in quadrat i . G_k is therefore the geometric mean of true negative and true positive rates for state k at observation i . Higher values represent better predictive performance, with a value of 1 indicating perfect categorisation of all observations within that density state. This measure penalises incorrect predictions for rarer states (i.e., high density states), which tend to have much higher true negative rates. We chose this metric as in imbalanced data, standard metrics are biased toward the majority class, as predicting the dominant class correctly contributes heavily to a high overall score. However, the geometric mean penalises poor performance on either class. If the model performs well on the majority class but poorly on the minority class (or vice versa), GMS will reflect this imbalance by yielding a low score.

To examine the field-level predictive performance compared to a baseline, we employed the ranked probability skill score [70] (RPSS). In this case, we compared classification accuracy to a naïve prediction made from the distribution of states across all fields used to train the model ensemble (i.e., state probabilities of H = 0.155, M = 0.157, L = 0.688). RPSS is derived from the ranked probability score (RPS):

$$RPS = \sum_{k=1}^K p_k - o_k(x) \quad (4)$$

where p_k and o_k denote predicted and observed probabilities for category k in quadrat x . RPSS is therefore

$$RPSS = 1 - \frac{\overline{RPS}}{\overline{RPS}_{baseline}} \quad (5)$$

where \overline{RPS} and $\overline{RPS}_{baseline}$ represent the average RPS across all quadrats in the validation set for the model predictions and naïve (baseline) classifier, respectively. Values above zero represent an improvement on the baseline classifier.

We compared changes in geometric mean scores and RPSS, to understand the effect of weightings on different feature sets. To identify the potential causes of predictive failure, we tested the effect of the median hypothesis margin distance to a field's nearest neighbour, and mean density state, on the change in RPSS at different values of α . The nearest neighbour distance may represent how similar new data are to the most similar field in the ensemble of classifiers. A large nearest neighbour distance may suggest that a field does not have good representation from the ensemble and could produce a higher prediction error. Mean density state is a measure of how severe the infestation in a field is; the variability in infestation severity might produce higher prediction errors as classifiers may have low accuracy for higher densities which were less well represented in our data. We tested these hypotheses using linear regression. We modelled the change in RPSS as a function of interactive effects between the feature set and weighting, with either nearest neighbour distance.

Data and code are available at the following repository: <https://doi.org/10.5061/dryad.qz612jmqp>.

3. Results

3.1. Within-Field vs. Out-of-Field Classification

The classifiers displayed good within-field accuracy (i.e., high GMS) for all density states (Figure 3A). All three density states displayed high levels of classification accuracy, with low and medium states being, on average, easier to predict than high states. On average, classifiers using the VGI feature set tended to have higher classification accuracy, although these differences were not statistically significant. When the ensembles of classifiers were used to predict observations from new fields, however, classification accuracy was poor (Figure 3B). Unweighted classifiers ($\alpha = 0$) displayed much lower classification accuracy scores than the within-field cross-validation exercise, with all classes' geometric mean score values decreasing from around 0.7 to 0.1 for low and high states. Medium state classification accuracy had slightly higher out-of-field accuracy scores (0.2) than high and low states, but still a large decrease from the within-field accuracy. Again, there were no clear differences in classification accuracy between the HS and VGI feature sets. The poor out-of-field performance is also evident using additional performance metrics (Figure S1).

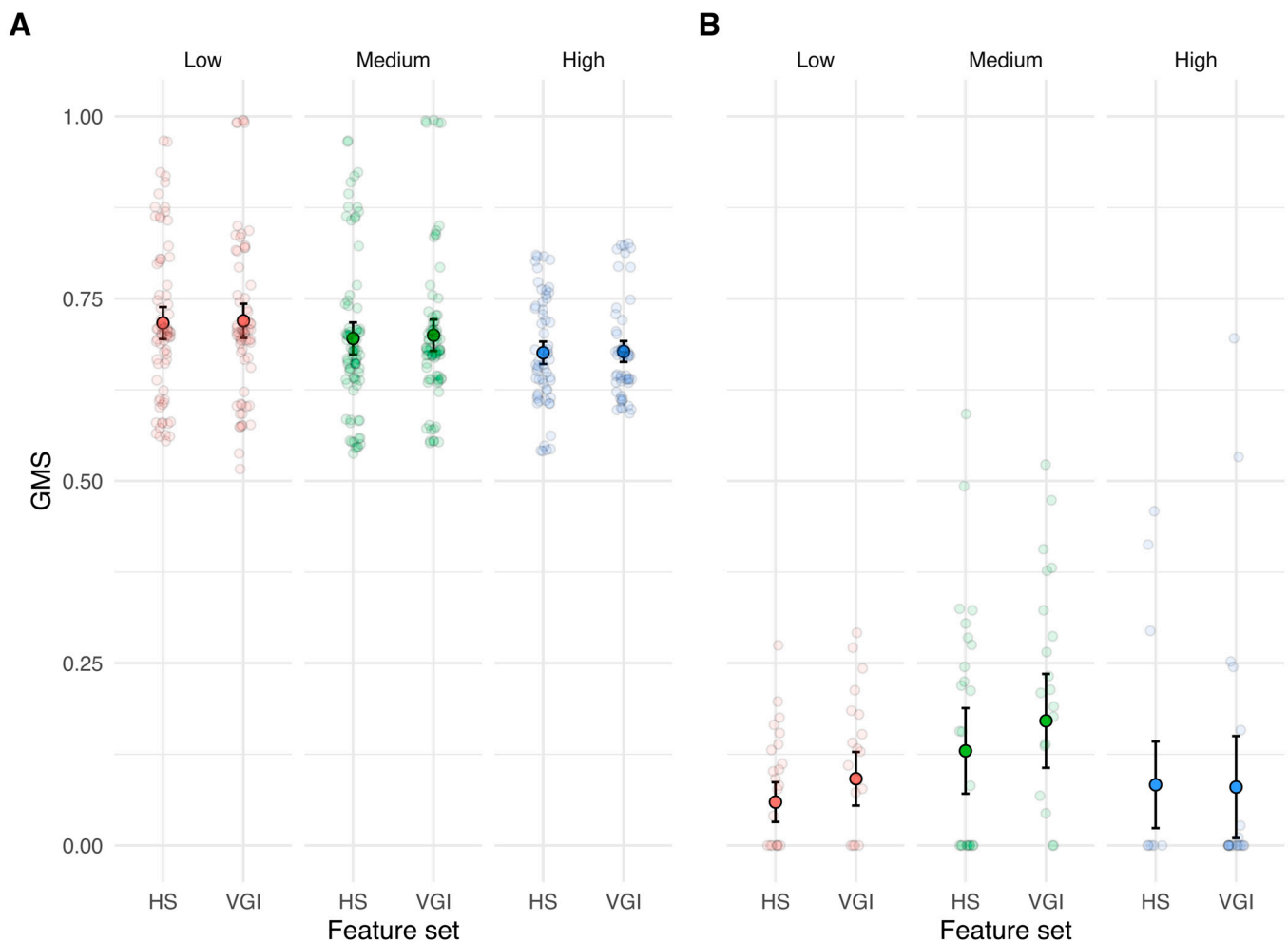


Figure 3. Within-field (A) and out-of-field (B) geometric mean scores (GMS) for Hyperspectral (HS) and vegetation index feature sets (VGI). Panels display scores for low, medium, and high density states, respectively. Point values are the average geometric mean score for predictions made to each quadrat within a field. Vertical bars are 95% confidence intervals. Faded coloured points in panel A are the accuracy scores for a single fold within a given field. Faded coloured points in panel B represent the average accuracy scores the ensemble made for a new field.

3.2. Ensemble Weighting

Average field-level RPSS demonstrated no improvement of model ensembles over a baseline naïve prediction drawn from the observed frequency of each density states (Figure 4). Indeed, unweighted ensembles and ensembles with low weightings ($\alpha = 2$) had, on average, worse predictions than the naïve classifier. The only ensemble that provided predictions that were on average on par with the naïve classifier was the ensemble with a high weighting using the VGI feature set.

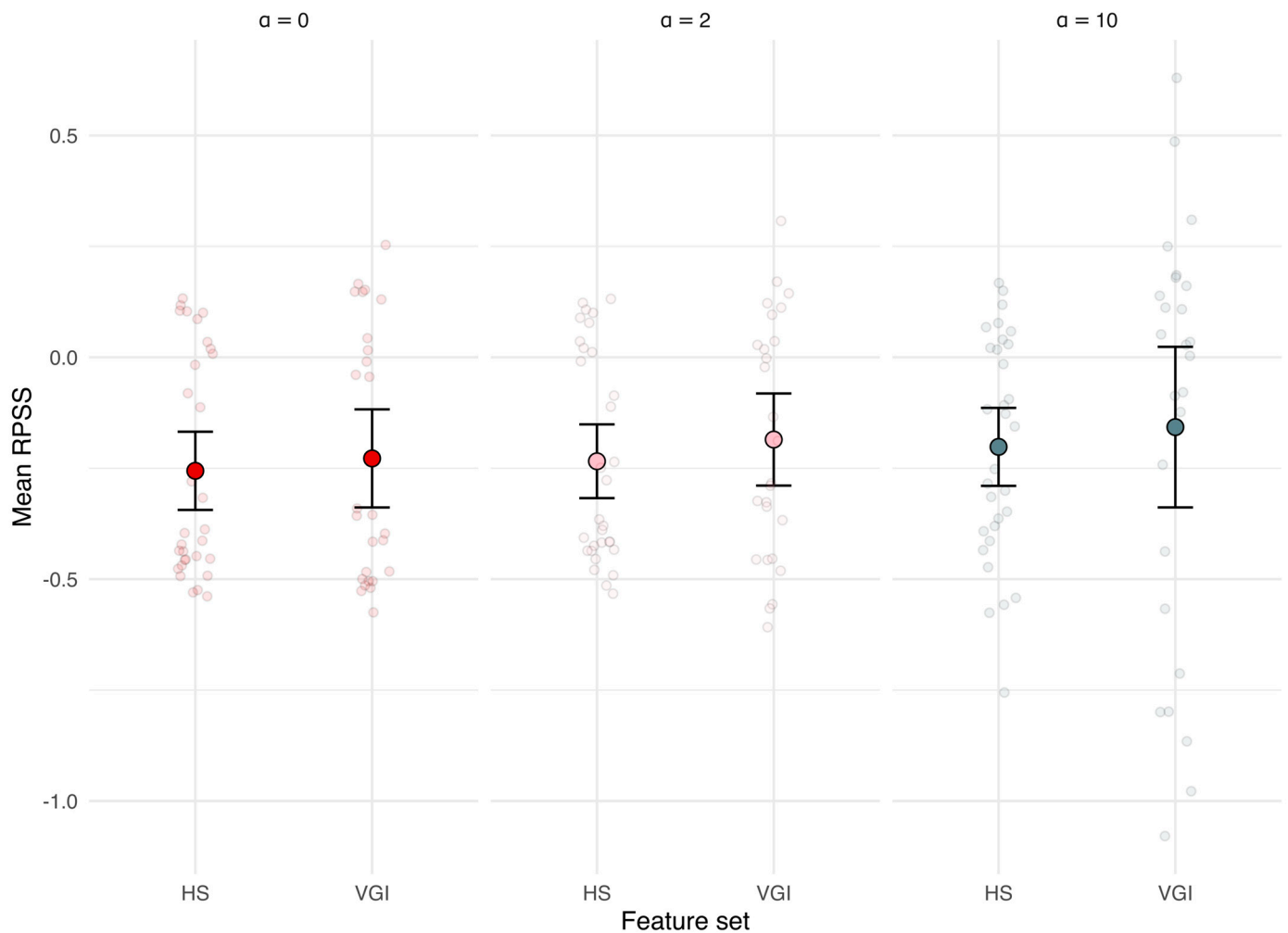


Figure 4. Out-of-field ranked probability skill scores (RPSS) for each feature set under different levels of α . α is the parameter controlling the size of the weights given to classifiers relative to the distance of the spectral signature of the classifier field and new data. A value of 0 indicates prediction accuracy was on par with the reference prediction. Point values are the average RPSS for all fields and vertical bars are 95% confidence intervals. Faded coloured points are the average RPSS the ensemble made for a new field.

On average, weighting classifiers marginally increased out-of-field classification accuracy for low density states for both feature sets (Figure 5A,B). Both weighting values ($\alpha = 2$, and $\alpha = 10$) increased accuracy scores by around 0.1 for both feature sets. Medium states, however, displayed no change in classification accuracy, with average changes being close to zero in both feature sets (Figure 5C,D); however, low weightings produced small decreases in accuracy. For the VGI feature set, both weightings increased classification accuracy, although only marginally for the low weighting value (Figure 5F). Conversely, for high density states, the low weighting produced no change in accuracy for

the HS feature set, whilst the high weighting produced a small decrease in classification accuracy (Figure 5E).

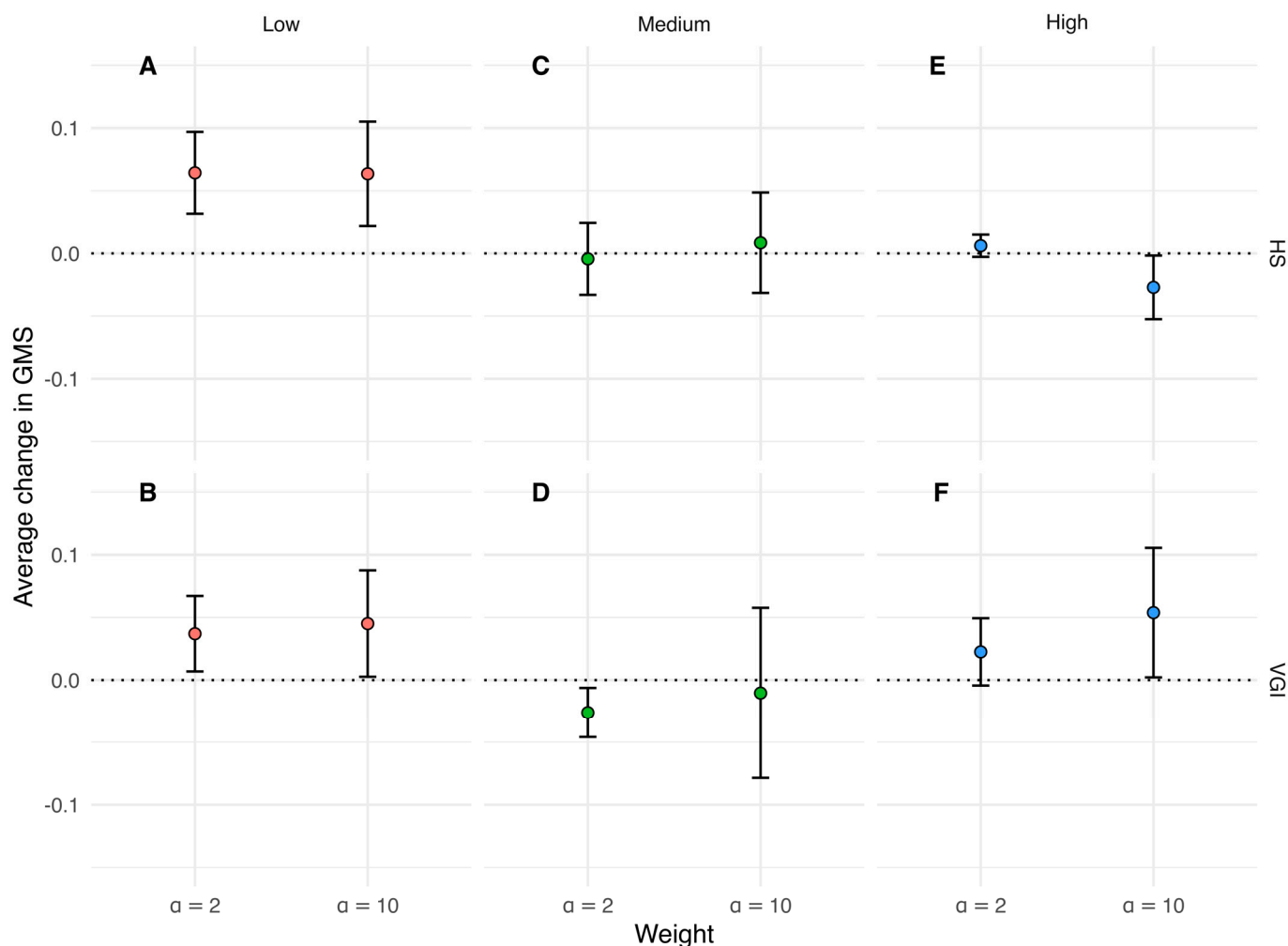


Figure 5. The average change in classification accuracy (change in geometric mean score-GMS) for hyperspectral (HS) and vegetation index (VGI) feature sets. Classification accuracy is presented for low (A,B), medium (C,D), and high (E,F) density states for different levels of α . α is the parameter controlling the size of the weights given to classifiers relative to the distance of the spectral signature of the classifier field and new data. Values over zero indicate an increase in accuracy, values below zero represent a decrease in accuracy. Point values are the change in average accuracy score for predictions made to each quadrat within a field. Vertical bars are 95% confidence intervals.

There was a wide distribution of changes in field-scale prediction accuracy under different weightings (Figure 6), but overall weighting predictions slightly increased field-scale accuracy for both feature sets. There was no detectable evidence of the nearest neighbour distance (Figure 7A) (linear model, $R^2 = 0.165$, $df = 5, 108$, $F = 4.251$) or mean density state (Figure 7B) (linear model, $R^2 = 0.022$, $df = 5, 108$, $F = 0.5$) on change in RPSS for any weighting or feature set combination.

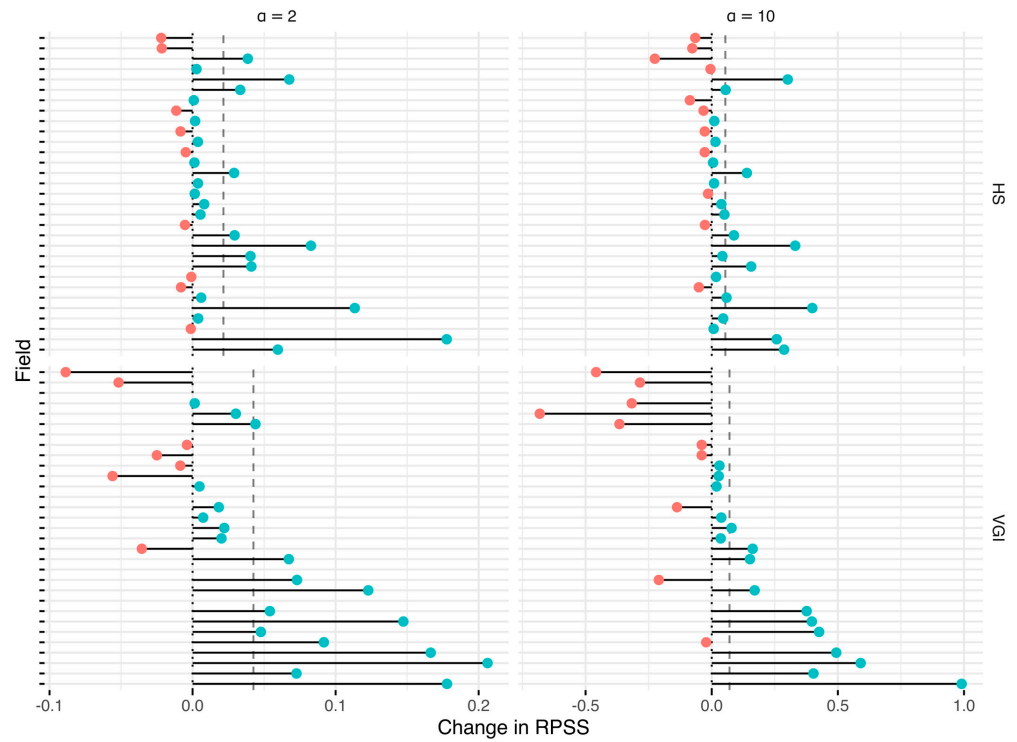


Figure 6. The change in RPSS for each field within our dataset for each value of α . Blue points over zero indicate an increase in field-scale predictive performance, red points below zero indicate a decrease in performance. Dashed vertical lines represent the average change in RPSS across all fields in each feature set and weighting. HS represents the hyperspectral feature set and VGI the vegetation index feature set.

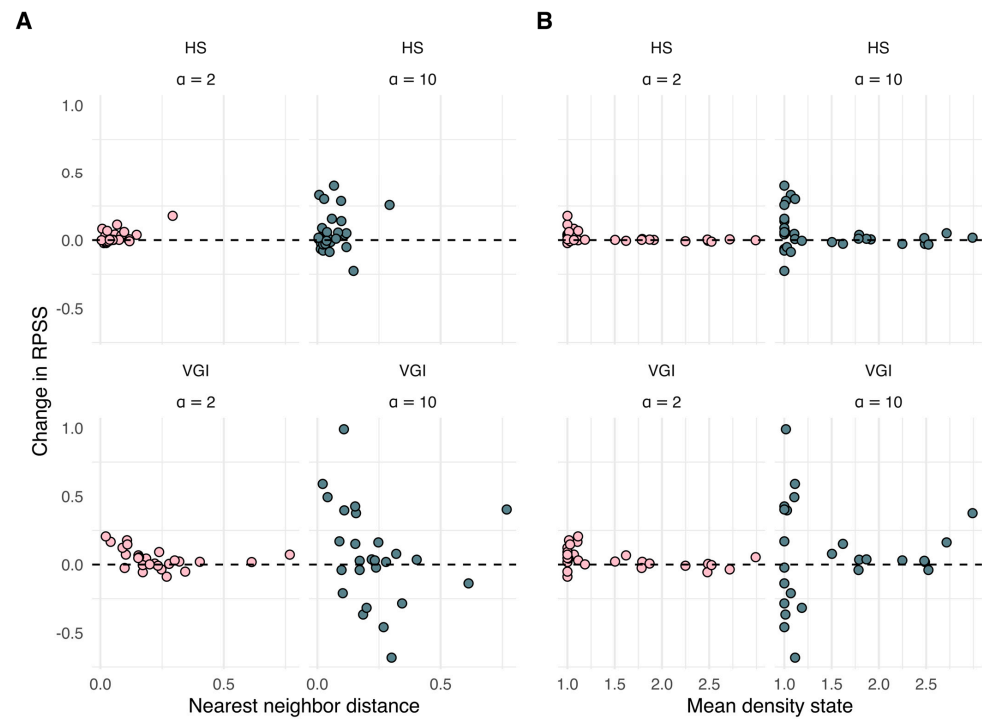


Figure 7. The change in RPSS versus the nearest neighbour distance (A) and mean density state of each field (B) for each value of alpha for both hyperspectral (HS) and vegetation index (VGI) feature sets. The nearest neighbour distance represents the median hypothesis margin distance to the nearest neighbour of a field, i.e., the field with the closest spectral similarity.

4. Discussion

The rapid and accurate identification and quantification of arable weed populations over large areas are important tasks for modern agriculture. Several studies have now shown that the combination of remote sensing data and machine learning provides a promising route to achieve mapping of weed populations over the scales relevant for management. However, making accurate predictions at new sites from limited training data is a stumbling block identified by several studies [14,15,71]. In this paper, we have demonstrated that increasing the coverage of spectral data alone is not enough to solve the issue, as predictive performance to new sites still displayed low predictive performance. We show that although classifiers demonstrated high accuracy when predicting for states gathered under static environmental conditions (i.e., at the same location and time), they failed to provide the same levels of accuracy when applied to data from new sites. We also demonstrated that although they provide flexibility and a route to improve predictive performance, using flexible ensemble techniques may decrease accuracy in certain situations, and as such should be approached with caution.

4.1. Ensemble Classification Using Hyperspectral Data

Hyperspectral imagery can provide a wealth of information for weed classification tasks. With a wider range of bandwidths and a higher spectral resolution comes the increased likelihood that data contains a spectral signal that can be used to identify the target organism in cases where target organisms and substrate are difficult to discriminate [26,44]. However, as we demonstrated here, accounting for the environmental variability in spectral data when predicting for new sites is still a key consideration, despite increased data quality. Interestingly there was little difference in performance between derived indices (VGI feature set) and normalised hyperspectral data (HS), as the VGI data consisted of features compiled from fewer spectral bands than the HS features. Investigation of custom indices tailored specifically for weed detection in arable crops in a variety of contexts would be a useful avenue for future research.

We employed a weighted ensemble of classifiers to increase the utility of a small dataset and accounted for environmental variability by weighting models towards fields with similar spectral properties. Our application demonstrated mixed results, displaying both increases and decreases in predictive performance, depending on the feature set employed to make the predictions. We demonstrated instances where weighting classifiers increased predictive power. However, our results showed that employing these techniques in practice should be approached with caution. Decreased predictive performance for high states (as is the case for the HS feature set, albeit marginally) is particularly detrimental to monitoring efforts, as high weed densities are of highest concern to farmers [46,48,72]. Given the current poor predictive performance of out-of-sample weed identification, we would recommend thorough testing of weighted ensemble techniques to determine the effect on predictive performance before employing them to identify weeds in practice.

4.2. Improving Performance-Quantification of a Spectral Signature

Given that there was no obvious relationship between predictive performance and mean density state or nearest neighbour distance of individual classifiers, it is highly likely that variability in the ambient light conditions across our fields was responsible for poor predictive performance. In this case, the temporally restricted data (i.e., single-date imagery) used in the majority of weed classification tasks [14,15,21,27–29,36,40–42] is likely the major obstacle limiting classification accuracy. The spectral signature of a plant is defined by traits such as the biochemical composition (e.g., water, pigment, nitrogen content etc) as well as the structural characteristics such as the shape and orientation of its leaves and stem [73]. As these characteristics co-vary with the temporal variation in light conditions, using temporally restricted observations will likely fail to characterise the radiative properties well enough to generalise to new dates or locations.

The identification of species-specific spectral signatures will therefore require quantification of the biochemical and structural variables that define them [73]. Radiative transfer models (RTMs) can provide a physical assessment of plant biological and structural properties that can define the spectral signature of target organisms [74–79]. Large-scale experimental work that aimed to quantify the relevant properties of specific weeds under varying light conditions could provide useful measures by which to identify and assess weeds in situ, but can also be achieved using remote sensing data. Work of this kind should be a priority for agricultural applications and many models have already been shown to define characteristics of many arable crops [80] but have yet to be applied to specific weed species.

As well as better quantification of spectral identifiers, it will be essential to increase the spatial and temporal scales of data collection to encompass a wider range of environmental conditions. Data collection technology is rapidly allowing the expansion of surveys across larger scales [81]. Satellite-based earth observation data often provide repeat measurements for observation units across a large spatial scale, and these data may provide a route to better data collection. However, there is a trade-off involved in the quality of data (in terms of bandwidth and spatial resolution) and many satellite-based data do not have the spatial resolution required to monitor small arable weeds and we are aware of no studies to date that have used satellite data to predict out-of-sample weed density accurately [82–85].

4.3. Improving Out-of-Field Performance Features and Algorithms

Although the most promising route to improving out-of-field prediction is to improve our quantification of spectral identifiers in tandem with upscaled data collection, there are other options that could provide modest improvements to current approaches. One option would be to invest more effort into the feature engineering steps of the analysis to buffer against environmental variability. As weeds typically exhibit patchy distributions within these survey sites [86], features that describe texture, rather than just raw spectral signals, could be a route to improving prediction and might be slightly buffered against ambient light levels [87]. LiDAR or point cloud data that distinguish varying canopy heights of crops and weeds might also be more robust to changes in ambient light levels. Data consistency might also be improved by using more rigorous atmospheric or topographic corrections, for example, to provide a more thorough route to removing illumination and atmospheric artefacts [88–90].

Noise reduction in current data is also an important consideration. More sophisticated learning algorithms that incorporate automated feature extraction are a possible route to reduce sample noise. Deep learning techniques such as convolutional neural networks (CNNs) might improve predictive performance, as they inherently account for spatial patterns in the data. Several studies have demonstrated their utility [15,29,38], showing high levels of within-field accuracy, yet still illustrate that out-of-field performance is relatively low. Another class of algorithms with promise are autoencoders, which are CNNs that are trained to ignore noise during the learning process [91]. This dimensionality reduction can then aid in subsequent classification steps [92]. Studies have already demonstrated their utility in detecting signals in noisy and high-dimensional ecological data [93] and they could provide a route to more efficient out-of-sample detection of black-grass infestations from high-dimension hyperspectral images. Combining deep learning techniques with GPU acceleration to increase both computation efficiency and data uptake is an important next step in out-of-sample weed detection in agriculture.

5. Conclusions

Overall, we demonstrate that providing generalisable predictions of black-grass density for new locations is a difficult task, even with the use of high-resolution and high-bandwidth spectral data. Employing flexible ensemble techniques did not provide conclusive improvements to performance, and in some cases decreased it. Although we suggest that future studies should target improved feature selection that incorporate spatial struc-

ture and textural metrics, it is important to emphasise that this alone might not solve the performance problem. A priority should be extensive data collection across the variable environments that exist in agricultural systems.

Supplementary Materials: The following supporting information can be downloaded at: <https://www.mdpi.com/article/10.3390/rs16244749/s1>. Figure S1. An illustration of the hierarchical clustering we used to determine the relationship between the number of density state observations in the 'Low' density class, and the spectral response of the vegetation indices. 16 VGIs are displayed, along the x axis (the blank entry represents VGIs not used in the classification task). Fields are displayed along the right hand axis. Lighter colours represent positive associations between the presence of the state and the index. Darker colours represent negative associations. The dendograms represent the clusters or similarity between indices (top tree) and spectral data within each field (left hand tree). The histogram illustrates the distribution of observations across the spectral response. Figure S2. An illustration of the hierarchical clustering we used to determine the relationship between the number of density state observations in the 'Medium' density class, and the spectral response of the vegetation indices. 16 VGIs are displayed, along the x axis (the blank entry represents VGIs not used in the classification task). Fields are displayed along the right hand axis. Lighter colours represent positive associations between the presence of the state and the index. Darker colours represent negative associations. The dendograms represent the clusters or similarity between indices (top tree) and spectral data within each field (left hand tree). The histogram illustrates the distribution of observations across the spectral response. Figure S3. An illustration of the hierarchical clustering we used to determine the relationship between the number of density state observations in the 'High' density class, and the spectral response of the vegetation indices. 16 VGIs are displayed, along the x axis (the blank entry represents VGIs not used in the classification task). Fields are displayed along the right hand axis. Lighter colours represent positive associations between the presence of the state and the index. Darker colours represent negative associations. The dendograms represent the clusters or similarity between indices (top tree) and spectral data within each field (left hand tree). The histogram illustrates the distribution of observations across the spectral response. Figure S4. Additional performance metrics for the out-of-field validation exercise for the HS (A), and VGI (B) feature sets. Faded coloured points represent the score for all predictions made by a single field-level classifier, large solid points represent the mean metric score over the ensemble. All predictions here are made by an unweighted classifier (i.e. $\alpha = 0$). Figure S5. Illustrations of spatial predictive performance from within-field classifications for an example field. Colour gradients either represent the predicted probability of a false positive (lighter green), or true positive (darker blue), for each density state. For example, for a low state (top left map), low states have higher probabilities of correct classifications are given dark blue colours, as evidenced by low states (l) mostly being dark blue. Whilst some medium states (m) are classified as false positives, having light green colours. Displayed on the maps are density state observations for a single field. Table S1. The hyper-parameter values across the optimization exercise were conducted. Table S2. Detailed specifications of the hyperspectral cameras used to collect images of fields containing weed infestations.

Author Contributions: Conceptualization, R.M.G., S.C., D.Z.C. and R.P.F.; methodology, R.M.G., S.C. and D.Z.C.; software, R.M.G. and S.C.; validation, R.M.G., S.C. and W.O.; formal analysis, R.M.G., S.C. and W.O.; resources, R.M.G., S.C. and W.O.; data curation, R.M.G., H.H. and D.C.; writing—original draft preparation, R.M.G. and S.C.; writing—review and editing, W.O., D.C., D.Z.C., H.H., W.O. and R.P.F.; visualisation, R.M.G.; supervision, D.Z.C. and R.P.F.; funding acquisition, D.Z.C. and R.P.F. All authors have read and agreed to the published version of the manuscript.

Funding: The black-grass network studied was established with funding from the Biotechnology and Biological Sciences Research Council (BBSRC; BB/L001489/1) and the Agriculture and Horticulture Development Board (AHDB) and is currently supported through the BBSRC 'Growing Health' (BB/X010953/1) Institute Strategic Programme. Data collection was supported by the Industrial Strategy Challenge Fund (ICSF) Seeding Award administered via the University of Sheffield.

Data Availability Statement: The data presented in this study are openly available in Data dryad at <https://doi.org/10.5061/dryad.qz612jmqp>.

Acknowledgments: We would like to thank the field assistants from Rothamsted Research that collected the density-state data and Laura Crook and Richard Hull for agronomical advice and help with data collection. Sejal Pramlall provided valuable advice on earth observation datasets.

Conflicts of Interest: Author William Oxford was employed by the company 2Excel Aviation Ltd. The remaining authors declare that the research was conducted in the absence of any commercial or financial relationships that could be construed as a potential conflict of interest.

References

- Lutman, P.J.W.; Moss, S.R.; Cook, S.; Welham, S.J. A review of the effects of crop agronomy on the management of *Alopecurus myosuroides*. *Weed Res.* **2013**, *53*, 299–313. [[CrossRef](#)]
- Goodsell, R.M.; Childs, D.Z.; Spencer, M.; Coutts, S.; Vergnon, R.; Swinfield, T.; Queenborough, S.A.; Freckleton, R.P. Developing hierarchical density-structured models to study the national-scale dynamics of an arable weed. *Ecol. Monogr.* **2021**, *91*, e01449. [[CrossRef](#)]
- Goodsell, R.M.; Comont, D.; Hicks, H.; Lambert, J.; Hull, R.; Crook, L.; Fraccaro, P.; Reusch, K.; Freckleton, R.P.; Childs, D.Z. Quantifying the impacts of management and herbicide resistance on regional plant population dynamics in the face of missing data. *J. Appl. Ecol.* **2024**, *61*, 1109–1126. [[CrossRef](#)]
- Buhler, D.D. Weed population responses to weed control practices. *Weed Sci. Soc. Am.* **1999**, *47*, 416–422. [[CrossRef](#)]
- Chauvel, B.; Guillemin, J.P.; Colbach, N.; Gasquez, J. Evaluation of cropping systems for management of herbicide-resistant populations of blackgrass. *Crop Prot.* **2001**, *20*, 127–137. [[CrossRef](#)]
- Daouti, E.; Jonsson, M.; Vico, G.; Menegat, A. Seed predation is key to preventing population growth of the weed *Alopecurus myosuroides*. *J. Appl. Ecol.* **2022**, *59*, 471–482. [[CrossRef](#)]
- Queenborough, S.A.; Burnet, K.M.; Sutherland, W.J.; Watkinson, A.R.; Freckleton, R.P. From meso- to macroscale population dynamics: A new density-structured approach. *Methods Ecol. Evol.* **2011**, *2*, 289–302. [[CrossRef](#)]
- Tredennick, A.T.; Hooten, M.B.; Aldridge, C.L.; Homer, C.G.; Kleinhesselink, A.R.; Adler, P.B. Forecasting climate change impacts on plant populations over large spatial extents. *Ecosphere* **2016**, *7*, e01525. [[CrossRef](#)]
- Freckleton, R.P.; Hicks, H.L.; Comont, D.; Crook, L.; Hull, R.; Childs, D.Z. Measuring the effectiveness of management interventions at regional scales by integrating ecological monitoring and modelling. *Pest Manag. Sci.* **2017**, *74*, 2287–2295. [[CrossRef](#)] [[PubMed](#)]
- Kleinhesselink, A.R.; Adler, P.B. The response of big sagebrush (*Artemisia tridentata*) to interannual climate variation changes across its range. *Ecology* **2018**, *99*, 1139–1149. [[CrossRef](#)]
- Shriver, R.K.; Andrews, C.M.; Pilliod, D.S.; Arkle, R.S.; Welty, J.L.; Germino, M.J.; Duniway, M.C.; Pyke, D.A.; Bradford, J.B. Adapting management to a changing world: Warm temperatures, dry soil, and interannual variability limit restoration success of a dominant woody shrub in temperate drylands. *Glob. Chang. Biol.* **2018**, *24*, 4972–4982. [[CrossRef](#)] [[PubMed](#)]
- Caughlin, T.T.; Damschen, E.I.; Haddad, N.M.; Levey, D.J.; Warneke, C.; Brudvig, L.A. Landscape heterogeneity is key to forecasting outcomes of plant reintroduction. *Ecol. Appl.* **2019**, *29*, e01850. [[CrossRef](#)] [[PubMed](#)]
- Damschen, E.I.; Brudvig, L.A.; Burt, M.A.; Fletcher, R.J.; Haddad, N.M.; Levey, D.J.; Orrock, J.L.; Resasco, J.; Tewksbury, J.J. Ongoing accumulation of plant diversity through habitat connectivity in an 18-year experiment. *Science* **2019**, *365*, 1478–1480. [[CrossRef](#)]
- Lambert, J.P.T.; Hicks, H.L.; Childs, D.Z.; Freckleton, R.P. Evaluating the potential of Unmanned Aerial Systems for mapping weeds at field scales: A case study with *Alopecurus myosuroides*. *Weed Res.* **2018**, *58*, 35–45. [[CrossRef](#)]
- Lambert, J.P.T.; Childs, D.Z.; Freckleton, R.P. Testing the ability of unmanned aerial systems and machine learning to map weeds at subfield scales: A test with the weed *Alopecurus myosuroides* (Huds). *Pest Manag. Sci.* **2019**, *75*, 2283–2294. [[CrossRef](#)]
- Weiss, M.; Jacob, F.; Duveiller, G. Remote sensing for agricultural applications: A meta-review. *Remote Sens. Environ.* **2020**, *236*, 111402. [[CrossRef](#)]
- Sant, E.D.; Simonds, G.E.; Ramsey, R.D.; Larsen, R.T. Assessment of sagebrush cover using remote sensing at multiple spatial and temporal scales. *Ecol. Indic.* **2014**, *43*, 297–305. [[CrossRef](#)]
- Thorp, K.R.; Tian, L.F. A Review on Remote Sensing of Weeds in Agriculture. *Precis. Agric.* **2004**, *5*, 477–508. [[CrossRef](#)]
- Zhang, C.; Atkinson, P.M.; George, C.; Wen, Z.; Diazgranados, M.; Gerard, F. Identifying and mapping individual plants in a highly diverse high-elevation ecosystem using UAV imagery and deep learning. *ISPRS J. Photogramm. Remote Sens.* **2020**, *169*, 280–291. [[CrossRef](#)]
- Baena, S.; Moat, J.; Whaley, O.; Boyd, D.S. Identifying species from the air: UAVs and the very high resolution challenge for plant conservation. *PLoS ONE* **2017**, *12*, e0188714. [[CrossRef](#)] [[PubMed](#)]
- Fraccaro, P.; Butt, J.; Edwards, B.; Freckleton, R.P.; Childs, D.Z.; Reusch, K.; Comont, D. A Deep Learning Application to Map Weed Spatial Extent from Unmanned Aerial Vehicles Imagery. *Remote Sens.* **2022**, *14*, 4197. [[CrossRef](#)]
- Tay, J.Y.L.; Erfmeier, A.; Kalwij, J.M. Reaching new heights: Can drones replace current methods to study plant population dynamics? *Plant Ecol.* **2018**, *219*, 1139–1150. [[CrossRef](#)]
- Martin, M. Cutadapt removes adapter sequences from high-throughput sequencing reads. *EMBnet J.* **2011**, *7*, 10–12. [[CrossRef](#)]

24. Rominger, K.; Meyer, S.E. Application of UAV-Based Methodology for Census of an Endangered Plant Species in a Fragile Habitat. *Remote Sens.* **2019**, *11*, 719. [[CrossRef](#)]
25. Andrew, M.E.; Ustin, S.L. The role of environmental context in mapping invasive plants with hyperspectral image data. *Remote Sens. Environ.* **2008**, *112*, 4301–4317. [[CrossRef](#)]
26. Papp, L.; van Leeuwen, B.; Szilassi, P.; Tobak, Z.; Szatmári, J.; Árvai, M.; Mészáros, J.; Pásztor, L. Monitoring invasive plant species using hyperspectral remote sensing data. *Land* **2020**, *10*, 29. [[CrossRef](#)]
27. Basinger, N.T.; Hestir, E.L.; Jennings, K.M.; Monks, D.W.; Everman, W.J.; Jordan, D.L. Detection of Palmer amaranth (*Amaranthus palmeri*) and large crabgrass (*Digitaria sanguinalis*) with in situ hyperspectral remote sensing. I. Effects of weed density and soybean presence. *Weed Sci.* **2022**, *70*, 198–212. [[CrossRef](#)]
28. Dmitriev, P.A.; Kozlovsky, B.L.; Kupriushkin, D.P.; Dmitrieva, A.A.; Rajput, V.D.; Chokheli, V.A.; Tarik, E.P.; Kapralova, O.A.; Tokhtar, V.K.; Minkina, T.M.; et al. Assessment of Invasive and Weed Species by Hyperspectral Imagery in Agroecosystem. *Remote Sens.* **2022**, *14*, 2442. [[CrossRef](#)]
29. Peteinatos, G.G.; Reichel, P.; Karouta, J.; Andújar, D.; Gerhards, R. Weed identification in Maize, sunflower, and potatoes with the aid of convolutional neural networks. *Remote Sens.* **2020**, *12*, 4185. [[CrossRef](#)]
30. Lopatin, J.; Dolos, K.; Kattenborn, T.; Fassnacht, F.E. How canopy shadow affects invasive plant species classification in high spatial resolution remote sensing. *Remote Sens. Ecol. Conserv.* **2019**, *5*, 302–317. [[CrossRef](#)]
31. Arroyo-Mora, J.P.; Kalacska, M.; Løke, T.; Schläpfer, D.; Coops, N.C.; Lucanus, O.; Leblanc, G. Assessing the impact of illumination on UAV pushbroom hyperspectral imagery collected under various cloud cover conditions. *Remote Sens. Environ.* **2021**, *258*, 112396. [[CrossRef](#)]
32. Motohka, T.; Nasahara, K.N.; Oguma, H.; Tsuchida, S. Applicability of Green-Red Vegetation Index for Remote Sensing of Vegetation Phenology. *Remote Sens.* **2010**, *2*, 2369. [[CrossRef](#)]
33. Paz-Kagan, T.; Silver, M.; Panov, N.; Karnieli, A. Multispectral Approach for Identifying Invasive Plant Species Based on Flowering Phenology Characteristics. *Remote Sens.* **2019**, *11*, 953. [[CrossRef](#)]
34. Meyer, H.; Reudenbach, C.; Wöllauer, S.; Nauss, T. Importance of spatial predictor variable selection in machine learning applications—Moving from data reproduction to spatial prediction. *Ecol. Model.* **2019**, *411*, 108815. [[CrossRef](#)]
35. Shahbazi, M.; Théau, J.; Ménard, P. Recent applications of unmanned aerial imagery in natural resource management. *GIScience Remote Sens.* **2014**, *51*, 339–365. [[CrossRef](#)]
36. Huang, Y.; Reddy, K.N.; Fletcher, R.S.; Pennington, D. UAV Low-Altitude Remote Sensing for Precision Weed Management. In *Weed Technology*; Cambridge University Press: Cambridge UK, 2018; pp. 2–6. [[CrossRef](#)]
37. Sulaiman, N.; Che'ya, N.N.; Mohd Roslim, M.H.; Juraimi, A.S.; Mohd Noor, N.; Fazlil Ilahi, W.F. The Application of Hyperspectral Remote Sensing Imagery (HRSI) for Weed Detection Analysis in Rice Fields: A Review. *Appl. Sci.* **2022**, *12*, 2570. [[CrossRef](#)]
38. Fricker, G.A.; Ventura, J.D.; Wolf, J.A.; North, M.P.; Davis, F.W.; Franklin, J. A convolutional neural network classifier identifies tree species in mixed-conifer forest from hyperspectral imagery. *Remote Sens.* **2022**, *11*, 2326. [[CrossRef](#)]
39. Underwood, E.; Ustin, S.; DiPietro, D. Mapping nonnative plants using hyperspectral imagery. *Remote Sens. Environ.* **2003**, *86*, 150–161. [[CrossRef](#)]
40. Thomas, L.-F.; Änäkälä, M.; Lajunen, A. Weakly Supervised Perennial Weed Detection in a Barley Field. *Remote Sens.* **2023**, *15*, 2877. [[CrossRef](#)]
41. Feng, C.; Zhang, W.; Deng, H.; Dong, L.; Zhang, H.; Tang, L.; Zheng, Y.; Zhao, Z. A Combination of OBIA and Random Forest Based on Visible UAV Remote Sensing for Accurately Extracted Information about Weeds in Areas with Different Weed Densities in Farmland. *Remote Sens.* **2023**, *15*, 4696. [[CrossRef](#)]
42. Guo, Z.; Cai, D.; Zhou, Y.; Xu, T.; Yu, F. Identifying rice field weeds from unmanned aerial vehicle remote sensing imagery using deep learning. *Plant Methods* **2024**, *20*, 105. [[CrossRef](#)]
43. Engler, R.; Waser, L.T.; Zimmermann, N.E.; Schaub, M.; Berdos, S.; Ginzler, C.; Psomas, A. Combining ensemble modeling and remote sensing for mapping individual tree species at high spatial resolution. *For. Ecol. Manag.* **2013**, *310*, 64–73. [[CrossRef](#)]
44. Feng, L.; Zhang, Z.; Ma, Y.; Du, Q.; Williams, P.; Drewry, J.; Luck, B. Alfalfa yield prediction using UAV-based hyperspectral imagery and ensemble learning. *Remote Sens.* **2020**, *12*, 2028. [[CrossRef](#)]
45. Freckleton, R.P.; Sutherland, W.J.; Watkinson, A.R.; Queenborough, S.A. Density-structured models for plant population dynamics. *Am. Nat.* **2011**, *177*, 1–17. [[CrossRef](#)]
46. Varah, A.; Ahodo, K.; Coutts, S.R.; Hicks, H.L.; Comont, D.; Crook, L.; Hull, R.; Neve, P.; Childs, D.Z.; Freckleton, R.P.; et al. The costs of human-induced evolution in an agricultural system. *Nat. Sustain.* **2020**, *3*, 63–71. [[CrossRef](#)] [[PubMed](#)]
47. Hicks, H.L.; Comont, D.; Coutts, S.R.; Crook, L.; Hull, R.; Norris, K.; Neve, P.; Childs, D.Z.; Freckleton, R.P. The factors driving evolved herbicide resistance at a national scale. *Nat. Ecol. Evol.* **2018**, *2*, 529–536. [[CrossRef](#)]
48. Varah, A.; Ahodo, K.; Childs, D.Z.; Comont, D.; Crook, L.; Freckleton, R.P.; Goodsell, R.; Hicks, H.L.; Hull, R.; Neve, P.; et al. Acting pre-emptively reduces the long-term costs of managing herbicide resistance. *Sci. Rep.* **2024**, *14*, 6201. [[CrossRef](#)] [[PubMed](#)]
49. SimActive. Correlator 3D, an Ultra-Rapid Solution for the Generation of Geospatial Data. 2018.
50. Schläpfer, D.; Schaepman, M.; Itten, K.I. PARGE: Parametric geocoding based on GCP-calibrated auxiliary data. In *Imaging Spectrometry IV*; SPIE: Bellingham, WA, USA, 1998; pp. 334–344.
51. Gitelson, A.A.; Merzlyak, M.N.; Chivkunova, O.B. Optical properties and nondestructive estimation of anthocyanin content in plant leaves. *Photochem. Photobiol.* **2001**, *74*, 38–45. [[CrossRef](#)] [[PubMed](#)]

52. Gitelson, A.A.; Zur, Y.; Chivkunova, O.B.; Merzlyak, M.N. Assessing carotenoid content in plant leaves with reflectance spectroscopy. *Photochem. Photobiol.* **2002**, *75*, 272–281. [[CrossRef](#)] [[PubMed](#)]
53. Gitelson, A.; Merzlyak, M.N. Quantitative estimation of chlorophyll-a using reflectance spectra: Experiments with autumn chestnut and maple leaves. *J. Photochem. Photobiol. B* **1994**, *22*, 247–252. [[CrossRef](#)]
54. Qi, J.; Chehbouni, A.; Kerr, Y.; Sorooshian, S. A modified soil adjusted vegetation index. *Remote Sens. Environ.* **1994**, *48*, 119–126. [[CrossRef](#)]
55. Rouse, J.W.; Haas, R.H.; Schell, J.A.; Deering, D.W. Monitoring Vegetation Systems in the Great Plains with ERTS. 1974. Available online: <https://ntrs.nasa.gov/citations/19740022614> (accessed on 23 September 2024).
56. Gamon, J.A.; Peñuelas, J.; Field, C.B. A narrow-waveband spectral index that tracks diurnal changes in photosynthetic efficiency. *Remote Sens. Environ.* **1992**, *41*, 35–44. [[CrossRef](#)]
57. Curran, P.; Windham, W.; Golz, H. Exploring the relationship between reflectance red edge and chlorophyll concentration in slash pine leaves. *Tree Physiol.* **1995**, *15*, 203–206. [[CrossRef](#)]
58. Penuelas, J.; Baret, F.; Filella, I. Semi-Empirical Indices to Assess Carotenoids/Chlorophyll-a Ratio from Leaf Spectral Reflectance. *Photosynthetica* **1995**, *31*, 221–230.
59. Haboudane, D.; Miller, J.R.; Pattey, E.; Zarco-Tejada, P.J.; Strachan, I.B. Hyperspectral vegetation indices and novel algorithms for predicting green LAI of crop canopies: Modeling and validation in the context of precision agriculture. *Remote Sens. Environ.* **2004**, *90*, 337–352. [[CrossRef](#)]
60. Rondeaux, G.; Steven, M.; Baret, F. Optimization of soil-adjusted vegetation indices. *Remote Sens. Environ.* **1996**, *55*, 95–107. [[CrossRef](#)]
61. Broge, N.H.; Leblanc, E. Comparing prediction power and stability of broadband and hyperspectral vegetation indices for estimation of green leaf area index and canopy chlorophyll density. *Remote Sens. Environ.* **2001**, *76*, 156–172. [[CrossRef](#)]
62. Vogelmann, J.E.; Rock, B.N.; Moss, D.M. Red edge spectral measurements from sugar maple leaves. *Int. J. Remote Sens.* **1993**, *14*, 1563–1575. [[CrossRef](#)]
63. Penuelas, J.; Pinol, J.; Ogaya, R.; Filella, I. Estimation of plant water concentration by the reflectance Water Index WI (R900/R970). *Int. J. Remote Sens.* **1997**, *18*, 2869–2875. [[CrossRef](#)]
64. Merzlyak, M.N.; Gitelson, A.A.; Chivkunova, O.B.; Rakitin, V.Y. Non-destructive optical detection of pigment changes during leaf senescence and fruit ripening. *Physiol. Plant.* **1999**, *106*, 135–141. [[CrossRef](#)]
65. Cloutis, E.; Connery, D.; Major, D.; Dover, F. Airborne multi-spectral monitoring of agricultural crop status: Effect of time of year, crop type and crop condition parameter. *Int. J. Remote Sens.* **1996**, *17*, 2579–2601. [[CrossRef](#)]
66. Gitelson, A.A.; Stark, R.; Grits, U.; Rundquist, D.; Kaufman, Y.; Derry, D. Vegetation and soil lines in visible spectral space: A concept and technique for remote estimation of vegetation fraction. *Int. J. Remote Sens.* **2002**, *23*, 2537–2562. [[CrossRef](#)]
67. Breiman, L. Random Forests. *Mach. Learn.* **2001**, *45*, 5–32. [[CrossRef](#)]
68. Wright, M.N.; Ziegler, A. Ranger: A fast implementation of random forests for high dimensional data in C++ and R. *J. Stat. Softw.* **2017**, *77*, 1–17. [[CrossRef](#)]
69. Gilad-Bachrach, R.; Navot, A.; Tishby, N. Margin based feature selection—Theory and algorithms. In *Twenty-First International Conference on Machine Learning—ICML '04*; ACM Press: Banff, AB, Canada, 2004; p. 43. [[CrossRef](#)]
70. Weigel, A.P.; Liniger, M.A.; Appenzeller, C. The Discrete Brier and Ranked Probability Skill Scores. *Mon. Weather. Rev.* **2007**, *135*, 118–124. [[CrossRef](#)]
71. Cox, J.; Li, X.; Fox, C.; Coutts, S. Black-grass (*Alopecurus myosuroides*) in cereal multispectral detection by UAV. *Weed Sci.* **2023**, *71*, 444–452. [[CrossRef](#)]
72. Ahodo, K.; Oglethorpe, D.; Hicks, H.L.; Freckleton, R.P. Estimating the farm-level economic costs of spring cropping to manage *Alopecurus myosuroides* (black-grass) in UK agriculture. *J. Agric. Sci.* **2019**, *157*, 318–332. [[CrossRef](#)]
73. Ollinger, S.V. Sources of variability in canopy reflectance and the convergent properties of plants. *New Phytol.* **2010**, *189*, 375–394. [[CrossRef](#)] [[PubMed](#)]
74. Shi, H.; Jiang, J.; Jacquemoud, S.; Xiao, Z.; Ma, M. Estimating leaf mass per area with leaf radiative transfer model. *Remote Sens. Environ.* **2023**, *286*, 113444. [[CrossRef](#)]
75. Jiang, J.; Comar, A.; Weiss, M.; Baret, F. FASPECT: A model of leaf optical properties accounting for the differences between upper and lower faces. *Remote Sens. Environ.* **2021**, *253*, 112205. [[CrossRef](#)]
76. Feret, J.-B.; François, C.; Asner, G.P.; Gitelson, A.A.; Martin, R.E.; Bidet, L.P.R.; Ustin, S.L.; Le Maire, G.; Jacquemoud, S. PROSPECT-4 and 5: Advances in the leaf optical properties model separating photosynthetic pigments. *Remote Sens. Environ.* **2008**, *112*, 3030–3043. [[CrossRef](#)]
77. Féret, J.-B.; Gitelson, A.A.; Noble, S.D.; Jacquemoud, S. PROSPECT-D: Towards modeling leaf optical properties through a complete lifecycle. *Remote Sens. Environ.* **2017**, *193*, 204–215. [[CrossRef](#)]
78. Féret, J.-B.; Berger, K.; de Boissieu, F.; Malenovský, Z. PROSPECT-PRO for estimating content of nitrogen-containing leaf proteins and other carbon-based constituents. *Remote Sens. Environ.* **2021**, *252*, 112173. [[CrossRef](#)]
79. S Jacquemoud; Baret, F. PROSPECT: A model of leaf optical properties spectra. *Remote Sens. Environ.* **1990**, *34*, 75–91. [[CrossRef](#)]
80. Xiang, S.; Jin, Z.; Li, J.; Yu, F.; Xu, T. RPIOSL: Construction of the radiation transfer model for rice leaves. *Plant Methods* **2024**, *20*, 1. [[CrossRef](#)]

81. Müllerová, J.; Brundu, G.; Große-Stoltenberg, A.; Kattenborn, T.; Richardson, D.M. Pattern to process, research to practice: Remote sensing of plant invasions. *Biol. Invasions* **2023**, *25*, 3651–3676. [[CrossRef](#)]
82. Singh, P.; Pandey, P.C.; Petropoulos, G.P.; Pavlides, A.; Srivastava, P.K.; Koutsias, N.; Deng, K.A.K.; Bao, Y. 8—Hyperspectral remote sensing in precision agriculture: Present status, challenges, and future trends. In *Hyperspectral Remote Sensing*; Pandey, P.C., Srivastava, P.K., Balzter, H., Bhattacharya, B., Petropoulos, G.P., Eds.; In Earth Observation; Elsevier: Amsterdam, The Netherlands, 2020; pp. 121–146. [[CrossRef](#)]
83. Simpson, M.D.; Akbari, V.; Marino, A.; Prabhu, G.N.; Bhowmik, D.; Rupavatharam, S.; Datta, A.; Kleczkowski, A.; Sujeetha, J.A.R.P.; Anantrao, G.G.; et al. Detecting Water Hyacinth Infestation in Kuttanad, India, Using Dual-Pol Sentinel-1 SAR Imagery. *Remote Sens.* **2022**, *14*, 2845. [[CrossRef](#)]
84. Matongera, T.N.; Mutanga, O.; Dube, T.; Sibanda, M. Detection and mapping the spatial distribution of bracken fern weeds using the Landsat 8 OLI new generation sensor. *Int. J. Appl. Earth Obs. Geoinform.* **2017**, *57*, 93–103. [[CrossRef](#)]
85. Tiwari, M.; Gupta, P.K.; Tiwari, N.; Chitale, S. Potential of temporal satellite data analysis for detection of weed infestation in rice crop. *Egypt. J. Remote Sens. Space Sci.* **2024**, *27*, 734–742. [[CrossRef](#)]
86. Rew, L.J.; Cousens, R.D. Spatial distribution of weeds in arable crops: Are current sampling and analytical methods appropriate? *Weed Res.* **2001**, *41*, 1–18. [[CrossRef](#)]
87. Rasti, P.; Ahmad, A.; Samiei, S.; Belin, E.; Rousseau, D. Supervised image classification by scattering transform with application to weed detection in culture crops of high density. *Remote Sens.* **2019**, *11*, 249. [[CrossRef](#)]
88. Qamar, F.; Dobler, G. Atmospheric correction of vegetation reflectance with simulation-trained deep learning for ground-based hyperspectral remote sensing. *Plant Methods* **2023**, *19*, 74. [[CrossRef](#)] [[PubMed](#)]
89. Xie, X.; Zhao, W.; Yin, G. TAVIs: Topographically Adjusted Vegetation Index for a Reliable Proxy of Gross Primary Productivity in Mountain Ecosystems. *IEEE Trans. Geosci. Remote Sens.* **2024**, *62*, 1–12. [[CrossRef](#)]
90. Jenerowicz, A.; Wierzbicki, D.; Kedzierski, M. Radiometric Correction with Topography Influence of Multispectral Imagery Obtained from Unmanned Aerial Vehicles. *Remote Sens.* **2023**, *15*, 2059. [[CrossRef](#)]
91. Borowiec, M.L.; Dikow, R.B.; Frandsen, P.B.; McKeeken, A.; Valentini, G.; White, A.E. Deep learning as a tool for ecology and evolution. *Methods Ecol. Evol.* **2022**, *13*, 1640–1660. [[CrossRef](#)]
92. Vincent, P.; Larochelle, H.; Lajoie, I.; Bengio, Y.; Manzagol, P.A.; Bottou, L. Stacked Denoising Autoencoders: Learning Useful Representations in a Deep Network with a Local Denoising Criterion. *J. Mach. Learn. Res.* **2010**, *11*, 3371–3408.
93. Rowe, B.; Eichinski, P.; Zhang, J.; Roe, P. Acoustic auto-encoders for biodiversity assessment. *Ecol. Inform.* **2021**, *62*, 101237. [[CrossRef](#)]

Disclaimer/Publisher’s Note: The statements, opinions and data contained in all publications are solely those of the individual author(s) and contributor(s) and not of MDPI and/or the editor(s). MDPI and/or the editor(s) disclaim responsibility for any injury to people or property resulting from any ideas, methods, instructions or products referred to in the content.